

Coaxial Airflow 2D Planar Simulation of Millifluidic Plant-Based Caviar Generator

Penjit Srinophakun, Anusith Thanapimmetha, Nutchapon Chiarasumran and Maythee Saisriyoot*
Department of Chemical Engineering, Faculty of Engineering, Kasetsart University, Bangkok, Thailand

Kittamet Chuwongbandith and Thongchai Rohitathisa Srinophakun
Department of Chemical Engineering, Faculty of Engineering, Kasetsart University, Bangkok, Thailand
Division of Sustainable and Resource Engineering, Faculty of Engineering, Kasetsart University, Bangkok, Thailand

* Corresponding author. E-mail: fengmts@ku.ac.th DOI: 10.14416/j.asep.2024.05.002
Received: 7 December 2023; Revised: 8 January 2024; Accepted: 29 January 2024; Published online: 29 May 2024
© 2024 King Mongkut's University of Technology North Bangkok. All Rights Reserved.

Abstract

Millifluidic plant-based caviar generator was investigated. Effects of parameters; continuous phase flow rate, dispersed phase flow rate, and dispersed phase aperture diameter on the equivalent diameter, degree of spherical shape, and generation rate in a coaxial airflow alginate droplet generator were examined using a computational fluid dynamics (CFD) simulation program. A 2D planar simulation together with the volume of fluid (VOF) was applied to describe the phenomenon of droplet generation. Results showed that increasing the continuous phase flow rate yielded a decrease in equivalent diameter but an increase in droplet generation rate and an increase in the degree of spherical shape. Increasing the dispersed phase flow rate yielded a decrease in the degree of spherical shape but a significant increase in the droplet generation rate as well as a slight increase in equivalent diameter. Increasing the dispersed phase aperture diameter yielded an increase in equivalent diameter but a decrease in droplet generation rate and degree of spherical shape. Overall, the device could generate from 1,400–9,000 drops per hour with around 2.3–4.0 mm in size.

Keywords: Bead generators, Caviar, Coaxial flow, Computational fluid dynamics, Volume of fluid

1 Introduction

Caviar refers to the eggs found in sturgeon fish, particularly those species native to the Caspian Sea [1], including Beluga, Sterlet, Kaluga hybrid [2], Osetra, Siberian sturgeon, and Sevruga. These eggs exhibit shades ranging from light to dark grey and possess a delicate, creamy flavor. Within traditional sturgeon fisheries, Beluga eggs (*Huso huso*) have an average size of 3.6–4.3 mm, Osetra (*Acipenser gueldenstaedtii*) eggs range from 3.2–3.8 mm, and Sevruga (*Acipenser stellatus*) eggs measure between 2.7–3.2 mm. For commonly cultured sturgeon species, White sturgeon (*Acipenser transmontanus*) eggs have sizes of 3.2–4.0 mm, and Siberian sturgeon (*Acipenser baerii*) eggs range from 2.4–3.0 mm. These caviar varieties are considered rare, expensive, and highly

regarded as delicacies within modern haute cuisine establishments. Nevertheless, there is a global trend of a significant decline in sturgeon productivity and stocks [3], primarily resulting from factors of anthropogenic, such as the violation of breeding and feeding conditions, unsustainable economic practices [4], [5], and environmental degradation [6].

Plant-based or vegan caviar has been recently developed for sustainable food with good nutrition, which is an alternative for future food and reduces caviar harvesting or sturgeon hunting. Caviar from plants is mostly produced from seaweed powder or seaweed fluid to be raw material mixed with a gelling agent such as sodium alginate, adding seasoning, flavor, and taste to create a dimension of flavor as close to caviar as feasible.

Sodium alginate, a natural polymer extracted

from brown seaweed, has a wide range of applications in food, pharmaceutical [7]–[9], and cosmetic industries as a thickener, stabilizer, and emulsifier [10]. This sodium salt of alginic acid can be water soluble and has the unique ability to form a gel when the solution contacts with divalent cations, for instance, calcium or magnesium ions. This technique has been extensively utilized in the food industry to produce gels, jellies [11], and encapsulations [12]. For alginate specification, the most widely used encapsulation technique is the bead generation method, which consists of dropping an aqueous solution of polymer and active ingredients into a gelling bath of calcium lactate.

Bead generators have been used and developed with various techniques to make them suitable for each job whether electrostatic [13], [14], vibration [15], [16], jet cutter [17], [18], coaxial flow [19]–[21] and there are many other types of bead generators [22]. Coaxial flow is one type of bead generators that is interesting in many scientific fields to generate small beads or droplets on the microscale in a spherical shape. This device can vary widely, but all involve a flowing disperse phase through a nozzle that is surrounded by a coaxial continuous phase flow. The continuous phase flow causes beads to be sheared rapidly from the nozzle where they fall into a bath of crosslinking/gelling solution. Several parameters in the coaxial flow droplet generator affect the droplet size, its generation rate, the shape of droplets, etc. Although the coaxial flow beads generator has been widely used in the microencapsulation field [23], [24], there is a challenge that arises for this research work to apply a coaxial flow device into the food field, by adapting the alginate droplet to be an alternative plant-based caviar.

This research proposes a millifluidic plant-based caviar generated from an airflow coaxial bead generator with the computational fluid dynamics (CFD)-simulation software [25]. The effects of the dispersed phase flow rate, the continuous phase flow rate, and the dispersed phase aperture size were investigated through 2D planar simulations aiming to create a bead size in the range of 2.5–3.5 mm analogous to real caviar.

2 Material and Methods

2.1 Alginate solution

The alginate solution was comprised mainly of 0.8%

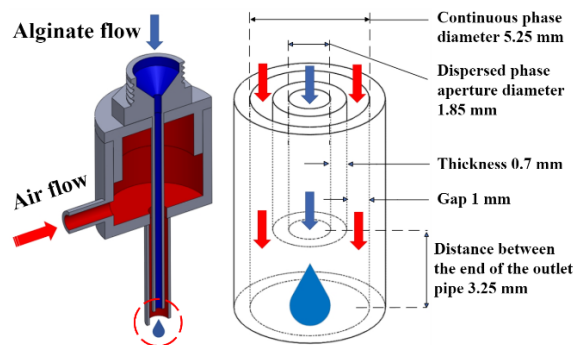


Figure 1: Coaxial airflow beads generator in the simulation.

sodium alginate and some plant-based additives. It was received from the Institute of Food Research and Product Development (IFRPD) at Kasetsart University. The surface tension between this solution and air was measured to be 70.69 mN/m. Alginate solution and air were used to simulate the droplet with coaxial airflow modeling. A rotating spindle viscometer (DRAWELL LVDV-2) was employed to measure the dynamic viscosity. The surface tension was analyzed by a surface tension meter (Kyowa Interface Science DY 300) with the Wilhelmy plate analyzing method. The pycnometer method was used to measure the density of the alginate solution. The density of alginate solution and air was 1,008.2 and 1.225 kg/m³. The dynamics viscosity was 3,147.9 and 1.7894 × 10⁻⁵ mPa·s.

2.2 Simulation process

Due to the requirement of around 3 mm of caviar size, the alginate tube aperture diameter of around 1.85 mm with 0.7 mm of thickness was used. The gap of the coaxial airflow was fixed at 1 mm, so the inside diameter of the air tube was 5.25 mm as illustrated in Figure 1. The walls of the flow domain were considered to have no-slip condition and wall roughness was set as a smooth wall. Surface tension modeling was considered. The isothermal state in all simulations was applied. The coaxial airflow bead generator used an air stream to promote droplet detachment which in turn, affected the diameter, generation rate, and spherical shape of the droplet.

In the simulation part, only the end of the coaxial airflow tube was used to study the effects of parameters with the computational fluid dynamic software. The

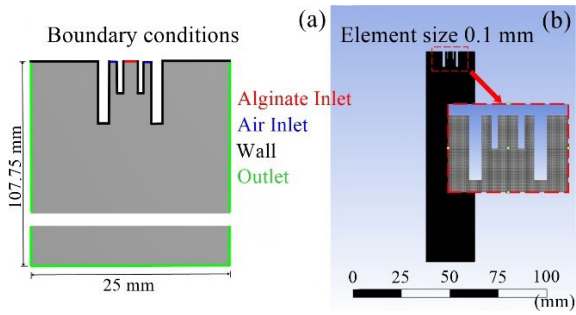


Figure 2: Boundary conditions (a) and mesh (b) in the simulation.

boundary conditions of the simulation were divided as alginate inlet, air inlet, wall, and outlet as illustrated in Figure 2. A coaxial airflow bead generator was simulated on a 2D planar ($25 \times 107.75 \text{ mm}^2$) with a face meshing method. The element size was 0.1 mm causing around 267,834 cells of meshing to be generated on a planar surface. Mesh quality was reported as orthogonal quality (Max: 0.99996 and Min: 0.99967) and skewness (Max: 0.01632 and Min: 1.3057×10^{-10}).

Grid independence tests were performed before the simulation procedure to guarantee optimal mesh spacing. All experimental simulations run under the Volume of Fluid (VOF) model in Ansys Fluent V19.2 by double-precision solvers. The primary phase and secondary phase were set to alginate solution and air. The flow was laminar setting by selecting the pressure-based type solver, and transient behavior. Gravity force was enabled at 9.806 m/s^2 . The explicit volume fraction was selected. The interface modeling was sharp/dispersed. The courant number was set at 0.25. Pressure-Implicit with Staggering Option (PISO) was selected as a scheme of the pressure velocity. PREssure STAggering Option (PRESTO!) and Green-Gauss Cell Based were selected in the spatial discretization in the solution method.

2.3 Roundness factor and equivalent diameter

The ImageJ analysis program was used to find the average area of the droplets leading to the determination of droplet volume by assuming every droplet was in perfect spherical shape ($V_{Img,J}$). The roundness factor was established to indicate the degree of the spherical shape of the droplet by comparing $V_{Img,J}$ with the average volume of droplets

$\left(V_{actual} = \frac{Q_{ag}}{N_d} \right)$ calculated from the droplet generation rate (N_d) and the alginate flow rate (Q_{ag}). If the roundness factor $\left(RF = \frac{V_{Img,J}}{V_{actual}} \right)$ was equal to 1, the shape of the droplet approached a perfect sphere. So, the equivalent diameter based on the droplet generation rate could be defined as $D_{eq} = 2 \cdot \sqrt[3]{\frac{3 \cdot V_{actual}}{4\pi}}$.

2.4 Numerical method

2.4.1 Simulation of coaxial flow

In the coaxial flow devices, both immiscible phase fluid or multiphase fluid including more than two phases such as liquid-liquid phase or liquid-gas phase were simulated by applying the VOF model [26]–[28]. In VOF formulation, the α_q is noted as q^{th} , the alginate fluid's volume fraction in the cell of coaxial flow. Three following conditions exist; $\alpha_q = 0$ (The cell is full of air); $\alpha_q = 1$ (The cell is full of alginate), and $0 < \alpha_q < 1$ (The cell contains the interface between the alginate and air). The simulation was conducted employing the VOF method utilizing an explicit scheme, representing a non-complexed simulation. The volume fraction equation was employed to track the alginate solution's fluid volume, and this was intricately combined with the momentum equation to compute the velocity field within the 2D planar model simulation. ANSYS FLUENT software was utilized for specifying the fluid properties and surface tension of the alginate solution, and subsequently, the corresponding equations, such as the surface tension equation, were employed for precise calculation. The details and description are available in the ANSYS FLUENT theory guide 14.0 [29].

2.4.2 Governing equations

The simulations used the VOF model in which the transport equation for the volume fraction of each phase was solved simultaneously with the continuity and momentum equations. The VOF model considers two or more immiscible fluids as one effective fluid in the whole domain in which the properties are

calculated as weighted averages based on the distribution of the volume fraction which is defined by Equation (1).

$$\sum_{p=1}^n \alpha_q = 1 \quad (1)$$

The continuity equation for the volume fraction of each one of the phases is defined by Equation (2).

$$\frac{1}{\rho_q} \left[\frac{\partial}{\partial t} (\alpha_q \rho_q) + \nabla \cdot (\alpha_q \rho_q \vec{v}_q) = \left[S_{\alpha_q} + \sum_{p=1}^n (\dot{m}_{pq} - \dot{m}_{qp}) \right] \right] \quad (2)$$

Where \dot{m}_{qp} is the mass transfer from phase q to phase p and \dot{m}_{pq} is the mass transfer from phase p to q phase. By default, the source term on the right-hand side of Equation (1), S_{α_q} is zero, but a constant or user-defined mass source for each phase can be specified.

A single momentum equation [Equation (3)] is solved throughout the domain, and the resulting velocity field is shared among the phases. The momentum equation, shown below, is dependent on the volume fractions of all phases through the properties ρ and μ :

$$\frac{\partial}{\partial t} (\rho \vec{v}) + \nabla \cdot (\rho \vec{v} \vec{v}) = -\nabla p + \nabla \cdot \left[\mu \left(\nabla \vec{v} + \nabla \vec{v}^T \right) \right] + \rho \vec{g} + \vec{F} \quad (3)$$

where ρ is the density; μ is the viscosity; ∇p is the pressure gradient; and g is the acceleration of gravity. The properties of the mixture, such as density and viscosity are calculated for the volume fraction and the properties of each phase x_q by Equation (4).

$$X = \sum \alpha_q x_q \quad (4)$$

According to the control volume formulation used by ANSYS FLUENT software, the convection and diffusion flux through the faces of the control volume are computed in the control volume and balanced with the source term. The calculation of face flux can be solved either through implicit or explicit time discretization.

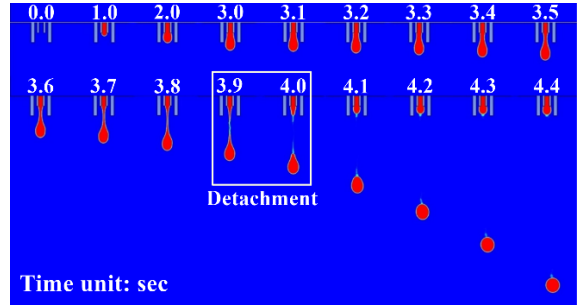


Figure 3: Coaxial airflow beads generator in the simulation.

2.4.3 The explicit scheme

An explicit time integration scheme utilizes the values at the current time step to estimate what will happen in the future. These values are then projected forward in time using the governing equations. These projections can be corrected or projected only a fraction of a time step forward to improve its accuracy.

Finite-difference interpolation schemes are applied to the volume fraction values that are computed at the previous time step as in Equation (5).

$$\frac{\alpha_q^{n+1} \rho_q^{n+1} - \alpha_q^n \rho_q^n}{\Delta t} V + \sum_f (\rho_q U_{j,f} \alpha_{q,f}^n) = \left[\sum_{p=1}^n (\dot{m}_{pq} - \dot{m}_{qp}) + S_{\alpha_q} \right] V \quad (5)$$

Where $n+1$ is an index for the new (current) time step; n is an index for the previous time step; V is a volume of cell; and $U_{j,f}$ is a volume flux through the face based on normal velocity.

3 Results and Discussion

3.1 Droplet detachment

The example of droplet formation from a simulation with 50 mL/h of alginate flow rate and 50 L/h of airflow rate is illustrated in Figure 3.

The alginate started to flow through the inside nozzle of the coaxial flow device at 0 seconds which is covered by the airflow outside. When the droplet starts to grow as illustrated in Figure 4, the droplet contact angle is less than the advancing contact angle

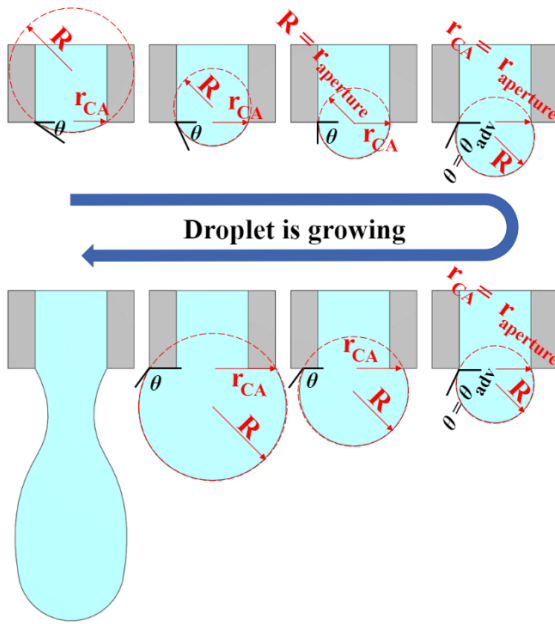


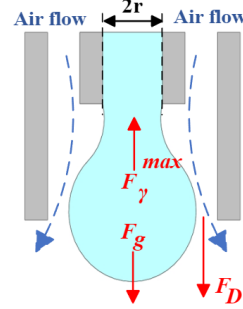
Figure 4: Droplet growth.

of the hydrophobic surface and the droplet contact radius (r_{CA}) equals the nozzle's inner aperture radius ($r_{aperture}$). The droplet contact line attaches to the inner side of the nozzle's aperture and the droplet contact angle grows until it reaches the surface advancing contact angle. When the droplet contact angle reaches the advancing contact angle of the surface, the droplet grows further while its contact angle is constant, and the droplet contact radius increases over the nozzle's inner aperture radius. Hence, the droplet contact area enlarges beyond the connected inner side of the nozzle's aperture. As the droplet grows farther, its surface separates from the end of the nozzle in the pendant form. At around 3.9 s the droplet detaches from its nozzle. After detachment, there is no capillary force acting on the droplet, thus the droplet tends to be pulled into a spherical shape by the cohesive forces of the surface layer over time.

Applying Tate's law [30], the droplet detaches the nozzle when the weight of the pendant drop (F_g) overcomes the maximum capillary force (F_γ^{max}) or $F_g > F_\gamma^{max}$. This assumption can be rewritten as in Equation (6).

$$\Delta\rho \frac{\pi}{6} d^3 g > 2f_{HB}\pi r\gamma \quad (6)$$

Forces acting on the droplet



Residue drop volume

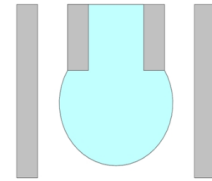


Figure 5: Droplet detachment.

Where $\Delta\rho$ is the relative density of alginate to air; r is the radius of the nozzle; γ is the surface tension between liquid and air; and f_{HB} is a constant value accounting for the liquid that remains attached to the nozzle after detachment occurs which is known as the Harkins-Brown correction factor [31], as illustrated in Figure 5.

By this idea, the droplet is held to the nozzle by the surface tension meanwhile its weight tries to draw it apart from the nozzle. In this scenario, the higher density of the alginate generates the higher weight of the pendant drop. Also, the viscosity ratio of the dispersed and continuous phases is one of the effective parameters in the dynamics of droplet generation [32]. Moreover, droplet sizes (d) can be controlled by the radius of the nozzle as $d \propto \sqrt[3]{r}$; however, decreasing droplet size by the radius of the nozzle has a limitation because reducing the radius of the nozzle affects the pressure drop over the nozzle itself as $\Delta P \propto \frac{1}{r^4}$. As a result, it is difficult to maintain a high droplet generation rate while its size is too small.

The airflow is employed to promote detachment. The airflow determines the drag force on the droplet which contributes to the downward force making the droplet detach easily. This drag force can be described as:

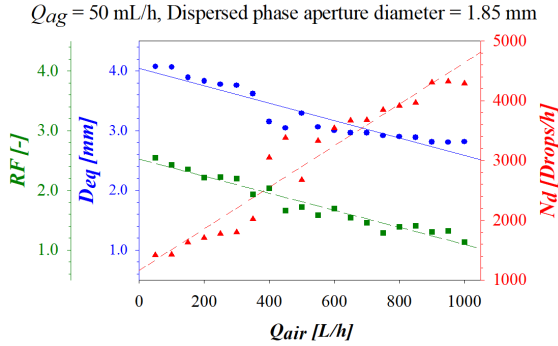


Figure 6: Effects of airflow rate.

$$F_D = 0.5C_D Au^2 \rho \quad (7)$$

Where ρ and u are the density and relative velocity of air to alginate; C_D is the drag coefficient; A is the cross-sectional area of a droplet ($A = \frac{1}{4}\pi d^2$). In this situation, the droplet size slowly increases as noticed from 1 s to 2 s and so on until the detachment occurred at around 3.9 s when the droplet weight combined with drag force F_D overcomes the maximum capillary force as:

$$F_g + F_D > f_{HB} F_\gamma^{\max} \quad (8)$$

3.2 Effects of airflow rate

Effects airflow rate in a range from 50 to 1,000 L/h (Reynolds number (Re) 285 to 5,697) with a fixed alginate flow rate of 50 mL/h (Re 0.003) was investigated. The airflow rate directly affected the equivalent diameter, roundness factor, and droplet generation rate according to the simulation results as illustrated in Figure 6.

The equivalent diameter of alginate beads decreased as the airflow rate increased. When the relative velocity of air to alginate (u in Equation (7)), the drag force also increased (F_D in Equation (7)), and when the drag force increased, the alginate solution detached from the aperture easily [Equation (8)] leading to a smaller droplet size generated [20], [24]. As a result, the droplet generation rate increased. However, the roundness factor decreased as the airflow rate increased implying that the shape of the droplet approached spherical shape because the smaller droplet size, the higher force of surface tension predominating

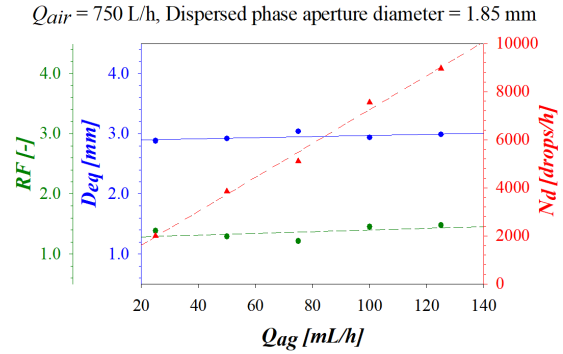


Figure 7: Effects of alginate flow rate.

the force of gravity, hence the droplet became more spherical.

This phenomenon was similar to the results from Lee *et al.*, [24] (continuous phase = 5–14 L/min resulting in 2.8–1.1 mm droplet size), Workamp *et al.*, [20] (continuous phase = 0, 3, 6 L/min resulting in 2.35, 1.5, 0.8 mm droplet size), Rahimi *et al.*, [33] (continuous phase = 1.5 to 6.5 mL/min resulting in 0.18 to 0.62 mm droplet size), and Deng *et al.*, [34] (continuous phase = 0.171 to 0.819 m/s resulting in 166.6 to 82 μm droplet size).

3.3 Effects of alginate flow rate

The influence of the dispersed phase flow rate in a range from 25 to 125 mL/h (Re 0.002 to 0.008) with a fixed airflow rate of 750 L/h (Re 4,273) was examined. The droplet generation rate of alginate beads increased as the alginate flow rate increased as illustrated in Figure 7. Unlike the effects of airflow rate, the equivalent diameter and roundness factor increased as the alginate flow rate increased. In the case of equivalent diameter, an increase in alginate flow rate led to the decrease of the relative velocity of air to alginate (u in Equation (7)), hence drag force (F_D in Equation (7)) also decreased. When the drag force decreased, the liquid detached from the aperture with difficulty [Equation (8)] leading to a bigger droplet size generated [20], [24]. However, the roundness factor increased as the alginate flow rate increased implying that the shape of the droplet departed from its spherical shape because the bigger the droplet size, the lower the force of surface tension predominating the force of gravity, hence the droplet became less spherical.

Moreover, the alginate flow rate had more influence on the equivalent diameter and roundness factor than the airflow rate did because the scale of the alginate flow rate was so far less than that of the airflow rate, so changing in alginate flow rate had less effect on the relative velocity of air to alginate (u in Equation (7)).

Many researchers also noticed this behavior including Lee *et al.* [24] (disperse phase 0.25 to 1.50 mL/min resulting in 1.15 to 1.25 mm droplet size and 5 to 18 beads/s generation rate), Deng *et al.* [34] (disperse phase 0.0066 to 0.2136 m/s resulting in 126.3 to 140.5 μm droplet size).

3.4 Effects of aperture size

In the case of the effects of aperture size represented by $D_{aperture}$ as illustrated in Figure 8(a), the phenomenon of droplet detachment was described differently from those of the alginate and airflow rates. The airflow rate, alginate flow rate and gap between the coaxial tube were fixed, therefore varying aperture size affected the velocities of both alginate and air phases. The alginate velocity $v_{alginate}$ exponentially reacted to aperture size

as $v_{alginate} \propto \frac{1}{D_{aperture}^2}$ while the air velocity (v_{air}) did not

$$\left(v_{air} \propto \frac{1}{(D_{aperture} + 2 \cdot Gab)^2} - \frac{1}{D_{aperture}^2} \right)$$

As formerly described, the velocity of air had more effect than that of alginate on the droplet size, so an increase in aperture size led to a decrease in both air and alginate velocities as illustrated in Figure 8 (b). However, again, the magnitude of the alginate flow rate was so far less than that of the airflow rate, that the relative velocity of air to alginate (u in Equation (7)) decreased as a result. This circumstance led the droplet weight combined with drag force to overcome the maximum capillary force easily [Equation (8)] leading to an increase of equivalent diameter. And when the equivalent diameter increased, the roundness factor increased consequently. However, responses of equivalent diameter and roundness factor were not parallel with each other, so the droplet generation rate did not linearly respond to aperture size. Deng *et al.*, [34], and Rahimi *et al.*, [33] investigated the effect of

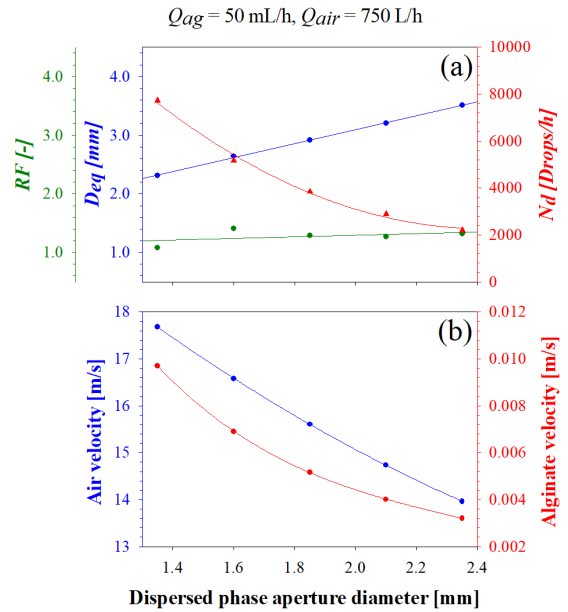


Figure 8: Effects of the dispersed phase aperture diameter.

nozzle diameter and reported that a larger droplet was also generated due to a larger nozzle size.

4 Conclusions

The droplet generation of millifluidic plant-based caviar at around 2.5–3.5 mm diameter was successfully simulated. The results were able to describe the relationship between the varying parameters. The dispersed phase flow rate had more effect than the continuous phase flow rate on the droplet generation rate. Nevertheless, the dispersed phase flow rate has almost no effect on the equivalent diameter and degree of spherical shape. In the case of dispersed phase aperture diameter, it had more effect on the droplet generation rate and equivalent diameter than on the degree of spherical shape. The study of a coaxial airflow with a 2D planar simulation model including the VOF method had enough capability for investigation and evaluation of the effects of the key parameters on the equivalent diameter and generation of droplet rate in this case. For better results, 3D simulations should be employed; however, they consume much computer resources for generated graphic results although giving a higher accuracy in dimension.

Acknowledgments

This work was financially supported by the National Science and Technology Development Agency (NSTDA); and the Faculty of Engineering, Kasetsart University, Bangkok, Thailand. The authors gratefully acknowledge the support of the Kasetsart University Research and Development Institute (KURDI); the WATA Cluster of computers; and the Institute of Food Research and Product Development (IFRPD) at Kasetsart University.

Author Contributions

All authors contributed to the study's conception and design; P.S., K.C., A.T., T.R.S., N.C., and M.S.: The analysis in each simulation was performed; M.S. and K.C.: The first draft of the manuscript was written; All authors commented on previous versions of the manuscript. All authors read and approved the final manuscript.

Conflicts of Interest

The authors declare no conflict of interest.

References

- [1] P. Bronzi, H. Rosenthal, and J. Gessner, "Global sturgeon aquaculture production: An overview," *Journal of Applied Ichthyology*, vol. 27, no. 2, pp. 169–175, 2011.
- [2] M. S. Chebanov, S. B. Podushka, E. I. Rachek, D. Y. Amvrosov, and Y. G. Merkulov, "Hybrids of the Siberian Sturgeon," in *The Siberian Sturgeon (Acipenser baerii, Brandt, 1869) Volume 2 – Farming*. Cham: Springer, pp. 289–326, 2018.
- [3] L. J. Graham and B. R. Murphy, "The decline of the beluga sturgeon: A case study about fisheries management," *Journal of Natural Resources and Life Sciences Education*, vol. 36, no. 1, pp. 66–75, 2007.
- [4] A. Raposo, H. A. Alturki, R. Alkutbe, and D. Raheem, "Eating Sturgeon: An Endangered Delicacy," *Sustainability*, vol. 15, no. 4, p. 3511, 2023.
- [5] D. L. Scarnecchia, Y. Lim, L. F. Ryckman, K. M. Backes, S. E. Miller, R. S. Gangl, and B. J. Schmitz, "Virtual population analysis, episodic recruitment, and harvest management of paddlefish with applications to other acipenseriform fishes," *Reviews in Fisheries Science & Aquaculture*, vol. 22, no. 1, pp. 16–35, 2014.
- [6] M. I. Mityagina, O. Y. Lavrova, and A. G. Kostianoy, "Main pattern of the caspian sea surface oil pollution revealed by satellite data," *Ecologica Montenegrina*, vol. 25, pp. 91–105, 2019.
- [7] M. A. J. Shaikh, K. S. Alharbi, W. H. Almalki, S. S. Imam, M. Albratty, A. M. Meraya, S. I. Alzarea, I. Kazmi, F. A. Al-Abbasi, O. Afzal, A. S. A. Altamimi, Y. Singh, S. K. Singh, K. Dua, and G. Gupta, "Sodium alginate based drug delivery in management of breast cancer," *Carbohydrate Polymers*, vol. 292, 2022, Art. no. 119689.
- [8] N. M. Sanchez-Ballester, B. Bataille, and I. Soulairol, "Sodium alginate and alginic acid as pharmaceutical excipients for tablet formulation: Structure-function relationship," *Carbohydrate Polymers*, vol. 270, 2021, Art. no. 118399.
- [9] M. F. Azhar, M. S. Haris, I. Mohamad, M. N. S. N. Ismadi, A. A. H. A. Yazid, S. R. Rahman, and N. H. M. Azlan, "Optimisation of alginate-pectin bead formulation using central composite design guided electrospray technique," *International Food Research Journal*, vol. 28, no. 4, pp. 860–870, 2021.
- [10] L. H. Pignolet, A. S. Waldman, L. Schechinger, G. Govindarajoo, J. S. Nowick, and T. Labuza, "The alginate demonstration: Polymers, food science, and ion exchange," *Journal of Chemical Education*, vol. 75, no. 11, 1998, doi: 10.1021/ed075p1430.
- [11] S. Patel, N. Scott, K. Patel, V. Mohylyuk, W. J. McAuley, and F. Liu, "Easy to swallow "Instant" jelly formulations for sustained release gliclazide delivery," *Journal of Pharmaceutical Sciences*, vol. 109, no. 8, pp. 2474–2484, 2020.
- [12] L. P. H. Bastos, J. Vicente, C. H. C. Santos, M. G. Carvalho, and E. E. Garcia-Rojas, "Encapsulation of black pepper (*Piper nigrum* L.) essential oil with gelatin and sodium alginate by complex coacervation," *Food Hydrocolloids*, vol. 102, 2020, Art. no. 105605.

- [13] D. Lewińska, J. Bukowski, M. Kozuchowski, A. Kinasiewicz, and A. Weryński, “Electrostatic microencapsulation of living cells,” *Biocybernetics and Biomedical Engineering*, vol. 28, pp. 69–89, 2008.
- [14] H. Watanabe, T. Matsuyama, and H. Yamamoto, “Experimental study on electrostatic atomization of highly viscous liquids,” *Journal of Electrostatics*, vol. 57, no. 2, pp. 183–197, 2003.
- [15] M. Whelehan and I. W. Marison, “Microencapsulation using vibrating technology,” *Journal of Microencapsulation*, vol. 28, no. 8, pp. 669–688, 2011.
- [16] Y. Zhou, S. Kajiyama, H. Masuhara, Y. Hosokawa, T. Kaji, and K. Fukui, “A new size and shape controlling method for producing calcium alginate beads with immobilized proteins,” *Journal of Biomedical Science and Engineering*, vol. 02, pp. 287–293, 2009.
- [17] S. Koch, C. Schwinger, J. Kressler, C. Heinzen, and N. G. Rainov, “Alginate encapsulation of genetically engineered mammalian cells Comparison of production devices, methods and microcapsule characteristics,” *Journal of Microencapsulation*, vol. 20, no. 3, pp. 303–316, 2003.
- [18] L. Martín-Banderas, A. M. Gañán-Calvo, and M. Fernández-Arévalo, “Making drops in microencapsulation processes,” *Letters in Drug Design & Discovery*, vol. 7, no. 4, pp. 300–309, 2010.
- [19] W. J. Aljohani, I. wenchao, M. W. Ullah, X. Zhang, and G. Yang, “Application of sodium alginate hydrogel,” *IOSR Journal of Biotechnology and Biochemistry*, vol. 03, no. 3, pp. 19–31, 2017.
- [20] M. Workamp, S. Alaie, and J. A. Dijkstra, “Coaxial air flow device for the production of millimeter-sized spherical hydrogel particles,” *Review of Scientific Instruments*, vol. 87, no. 12, 2016, Art. no. 125113.
- [21] G. V. Theodorakopoulos, F. K. Katsaros, S. K. Papageorgiou, M. Beazi-Katsioti, and G. E. Romanos, “Engineering commercial TiO₂ powder into tailored beads for efficient water purification,” *Materials (Basel)*, vol. 15, no. 1, p. 326, 2022.
- [22] R. K. Reddy, J. Gupta, and P. Izharuddin, “Alginate microspheres: The innovative approaches to production of the microbeads/micro-particles,” *Journal of Drug Delivery and Therapeutics*, vol. 9, no. 4-s, pp. 774–781, 2019.
- [23] T. Andersen, P. Auk-Emblem, and M. Dornish, “3D cell culture in alginate hydrogels,” *Microarrays (Basel)*, vol. 4, no. 2, pp. 133–161, 2015.
- [24] D. Lee, S. E. Greer, M. A. Kuss, Y. An, and A. T. Dudley, “3D printed alginate bead generator for high-throughput cell culture,” *Biomed Microdevices*, vol. 23, no. 2, p. 22, 2021.
- [25] V. Kunopagarnwong, T. Rohitatisa Srinophakun, T. Sritaweewat, and Y. Chisti, “Design of a stacked-layer tubular photobioreactor for microalgae cultivation,” *KMUTNB International Journal of Applied Science and Technology*, vol. 8, no. 3, pp. 179–184, 2015.
- [26] F. Guo and B. Chen, “Numerical study on Taylor bubble formation in a micro-channel T-junction using VOF method,” *Microgravity Science and Technology*, vol. 21, no. S1, pp. 51–58, 2009.
- [27] M. W. Weber and R. Shandas, “Computational fluid dynamics analysis of microbubble formation in microfluidic flow-focusing devices,” *Microfluidics and Nanofluidics*, vol. 3, no. 2, pp. 195–206, 2006.
- [28] F. Mardani, S. Falahatian, and M. Taghipoor, “Mapping flow-focusing microfluidic droplet formation to determine high-throughput droplet generation configurations,” *Results in Engineering*, vol. 18, 2023, Art. no. 101125.
- [29] *Ansys Fluent 14.0 Theory Guide*, Ansys, Pennsylvania, USA, 2011.
- [30] T. Tate, “XXX. On the magnitude of a drop of liquid formed under different circumstances,” *The London, Edinburgh, and Dublin Philosophical Magazine and Journal of Science*, vol. 27, no. 181, pp. 176–180, 1864.
- [31] W. D. Harkins and F. E. Brown, “The determination of surface tension (free surface energy) and the weight of falling drops: The surface tension of water and benzene by the capillary height method,” *Journal of the American Chemical Society*, vol. 41, no. 4, pp. 499–524, 1919.
- [32] J. Yao, F. Lin, H. S. Kim, and J. Park, “The effect of oil viscosity on droplet generation rate and droplet size in a T-junction microfluidic droplet generator,” *Micromachines (Basel)*, vol. 10, no. 12, p. 808, 2019.



- [33] M. Rahimi, A. Shams Khorrami, and P. Rezai, "Effect of device geometry on droplet size in co-axial flow-focusing microfluidic droplet generation devices," *Colloids and Surfaces A: Physicochemical and Engineering Aspects*, vol. 570, pp. 510–517, 2019.
- [34] C. Deng, H. Wang, W. Huang, and S. Cheng, "Numerical and experimental study of oil-in-water (O/W) droplet formation in a co-flowing capillary device," *Colloids and Surfaces A: Physicochemical and Engineering Aspects*, vol. 533, pp. 1–8, 2017.